Surface Fluxes and Boundary Layer Recovery in TOGA COARE: Sensitivity to Convective Organization

THOMAS R. SAXEN AND STEVEN A. RUTLEDGE

Department of Atmospheric Science, Colorado State University, Fort Collins, Colorado

(Manuscript received 14 April 1997, in final form 27 January 1998)

ABSTRACT

Shipboard radar data collected during the Tropical Ocean Global Atmosphere Coupled Ocean–Atmosphere Response Experiment (TOGA COARE) are used in conjunction with surface meteorological data from the Woods Hole Oceanographic Institute's IMET buoy to describe in detail how three classifications of convective systems modify the surface fluxes of heat, moisture, and momentum. The classifications of convection were based on spatial-scale [sub–mesoscale convective system (MCS) vs MCS scale], horizontal morphology (nonlinear vs linear organization), and the presence of stratiform precipitation as determined by quantitative radar data. Three types of convective organization were examined; sub-MCS-scale nonlinear events and MCS-scale linear events with and without significant stratiform precipitation. These three classifications were present about 90% of the time and produced over 90% of the rainfall during TOGA COARE, as determined by shipboard radar. Composite analyses of the surface fluxes along with the pertinent bulk variables have been constructed for each of these classes of convective organization. During the compositing process, the convectively active and recovery periods were separated, allowing these distinctly different phases to both be represented in the final composite analyses. The sensible and latent heat flux enhancements were decomposed through perturbation analyses and the relative importance of each term during the convectively active and recovery phases was also assessed.

All three types of convective organization altered the surface fluxes in a similar manner, producing greatly enhanced surface fluxes during the convectively active phase with weaker enhancements during the recovery. However, the duration of the convectively active and recovery phases were highly dependent on the type of convective organization that was present. The average length of the convectively active phase ranged from approximately 45 min for MCS-scale linear events that had little stratiform precipitation to about 1.5 h for MCS-scale linear events with extensive stratiform regions. The average length of the recovery phase was approximately 3.5 h for sub-MCS-scale nonlinear events, 2.5 h for MCS-scale linear events with little stratiform precipitation, and nearly 9.5 h for the MCS-scale linear events with extensive stratiform areas.

The magnitudes of the surface fluxes were also highly dependent on the mode of convective organization. The MCS-scale linear systems that had extensive stratiform precipitation were indicative of highly organized and mature squall line systems and hence produced the greatest modulations of the surface fluxes. These events produced peak sensible and latent heat fluxes of about 60 W m^{-2} and 250 W m^{-2}, respectively. The sub-MCS-scale nonlinear events and the MCS-scale linear events with little stratiform precipitation produced much weaker peak sensible and latent heat fluxes (about 20 W m^{-2} and 150 W m^{-2}, respectively). For all three types of convective organization the enhanced sensible heat fluxes were due primarily to increased air–sea temperature differences (i.e., decreased air temperature) and increased wind speeds. Approximately two-thirds of the total enhanced sensible heat transfer occurred during the recovery phase for each type of convective organization. For the sub-MCS-scale nonlinear events and MCS-scale linear events with little stratiform precipitation, the latent heat flux enhancements were due primarily to increased wind speeds. Increased wind speeds were also the primary contributor to the enhanced latent heat fluxes for the MCS-scale linear events with extensive stratiform precipitation, but increases in the air–sea humidity difference and the transfer coefficient for moisture also contributed. For the MCS-scale events, the enhanced latent heat transfer was split nearly evenly between the convectively active and recovery phases, whereas for the sub-MCS-scale nonlinear event, nearly 60% of the enhanced latent heat transfer occurred during the convectively active phase compared to about 40% during the recovery phase.

1. Introduction

The observational phase of the Tropical Ocean Global Atmosphere Coupled Ocean–Atmosphere Response Experiment (TOGA COARE) took place in the western Pacific warm pool from November 1992 through March 1993. This is one of the most convectively active regions of the world, receiving an estimated 3–5 m of rainfall each year (Taylor 1973) and it is known that convectively driven circulations have pronounced effects at the ocean surface. As an example, convective-scale downdrafts transport air from the lower to middle troposphere down to the surface (Zipser 1969, 1977; Gamache and

Corresponding author address: Dr. Steven A. Rutledge, Dept. of Atmospheric Science, Colorado State University, Ft. Collins, CO 80523.
E-mail: rutledge@olympic.atmos.colostate.edu

Houze 1982). The air within these drafts is generally cooler and drier than the environmental surface air. The divergent nature of these drafts at the surface also promotes fluctuations in the surface wind speed (Addis et al. 1984). Collectively these processes lead to significant surface fluxes of heat, moisture, and momentum; the processes by which the ocean and the atmosphere interact with each other. The overarching goal of TOGA COARE was to provide a better understanding of the fundamental processes responsible for ocean–atmosphere coupling in the tropical western Pacific (Webster and Lukas 1992). Therefore, a central goal of COARE was to provide a detailed description of the effects that atmospheric convective systems have on surface fluxes of heat, moisture, and momentum.

A number of previous studies have addressed the modulation of surface fluxes by convection. During the GARP (Global Atmospheric Research Program) Atlantic Tropical Experiment (GATE), Gaynor and Ropelewski (1979) found a convectively modified boundary layer about 30% of the time. In their analysis of 137 disturbances, Gaynor and Ropelewski found that in the region of the atmospheric density current (or cold pool), the surface sensible heat flux was clearly enhanced. However, they did not find any conclusive changes in the latent heat flux or wind stress. Johnson and Nicholls (1983) analyzed an intense GATE squall line and found a dramatic increase in the sensible heat flux in the region of the cold pool, in addition to significant increases in the latent heat flux.

Barnes and Garstang (1982) used data collected during GATE to analyze convectively driven modifications of the atmospheric boundary layer through moist static energy arguments. In light rain cases, they found that changes in the moist static energy were small because the drop in air temperature was nearly balanced by an increase in specific humidity. Barnes and Garstang hypothesized that these cases lacked strong, penetrative convective-scale downdrafts, which would have brought cool, drier air to the surface. The heavy rain cases, which they hypothesized had penetrative downdrafts, showed a distinct drop in moist static energy due to the combined effects of a reduced air temperature and specific humidity.

Jabouille et al. (1996) used a cloud-resolving model to simulate two convective events that were observed during TOGA COARE. The resulting surface flux enhancements were similar for both cases with latent and sensible heat flux enhancements of approximately 200% and 300%, respectively. Jabouille et al. found that the latent heat flux enhancements were generally limited to the regions of active convection, whereas the sensible heat flux enhancements occurred over a much larger area. Wind speed enhancements were generally confined to the region of the convective outflow, which in turn confined the increases in latent heat flux to this area. The sensible heat flux, on the other hand, was enhanced not only by increased wind speeds, but also by the drop in air temperature that can occur throughout the region of rainfall.

Young et al. (1995) analyzed the wakes of 42 convective events in the tropical western Pacific using hourly averaged data collected on the R/V *Wecoma* during a COARE pilot cruise and on the R/V *Moana Wave* during TOGA COARE. They produced composite time series of a number of atmospheric variables to describe the evolution of convective wakes, concentrating on the boundary layer's response to large mesoscale convective systems (MCSs). Young et al. found the average duration of the convective wake to be 12.7 h, with the surface fluxes being markedly enhanced in response to atmospheric convection. They found that the latent heat flux, sensible heat flux, and wind stress increased by 50%–100%, 300%, and 200%–500%, respectively. They attributed the enhanced latent heat flux and wind stress to increased wind speeds resulting from convective-scale downdrafts, whereas the enhanced sensible heat flux was attributed to the combined effects of enhanced wind speed and a distinct drop in air temperature.

All of these previous studies have shown that the effects of atmospheric convection lead to an enhancement in the surface fluxes. However, none of these studies systematically determined how the modification of surface fluxes varied with convective organization. Rickenbach and Rutledge (1998) used radar reflectivity data to identify different types of convective organization during TOGA COARE. Their classification scheme was based on the spatial scale and horizontal morphology of the convective system. The primary objective of this study is to describe in detail how the identified types of convective organization modify the surface fluxes of heat, moisture, and momentum. To achieve this goal, a composite analysis of the surface fluxes, along with the pertinent bulk variables (e.g., wind speed, air temperature, and SST), was developed for three classifications of convective organization. The three convective classifications used represent the two dominant convective modes identified by Rickenbach and Rutledge: sub-MCS-scale nonlinear and MCS-scale linear events. The MCS-scale linear events were further subdivided based on the presence of trailing stratiform precipitation. The composites were the product of many individual time series, stratified by convective organization. During the compositing process, the convectively active and boundary layer recovery time periods were separated so that the distinctly different processes occurring during the two phases would be accurately represented in the final composites. A second objective of the present study is to quantify the contributions to the sensible and latent heat flux enhancements associated with variations in the respective bulk variables and transfer coefficients for the three types of convective systems. A perturbation analysis was performed to achieve this goal. The relative importance of the en-

TABLE 1. IMET buoy instrumentation (Weller and Anderson 1996).

Parameter	Instrument	Sensor height
Air temperature	Thermistor with gill shield	2.78 m
SST	Thermistor	−0.45 m
Wind speed and direction	R. M. Young cup/vane	3.54 m
Barometric pressure	Paroscientific digiquartz	3.00 m
Relative humidity	Vaisala humicap with gill shield	2.74 m
Incoming shortwave radiation	Eppley precision spectral pyranometer (PSP)	3.54 m
Incoming longwave radiation	Eppley precision infrared radiometer (PIR)	3.54 m

hanced heat transfer during the convectively active and recovery phases is also addressed.

2. Methodology

a. Data

This study focuses on analysis of radar reflectivity data collected by the Massachusetts Institute of Technology (MIT) C-band Doppler radar onboard the R/V *Vickers* research vessel during COARE, in conjunction with surface meteorological data from the Woods Hole Institute of Oceanography Improved Meteorology (IMET) buoy. Rutledge et al. (1993) and Short et al. (1997) provided a discussion of the MIT radar deployment during COARE. The R/V *Vickers* was positioned near 2°05′S, 156°15′E for three 30-day deployments during which the MIT radar operated nearly continuously. Cruise 1 was approximately from 10 November to 10 December 1992, cruise 2 covered 21 December 1992 to 19 January 1993, and cruise 3 covered 29 January through 25 February 1993. Radar reflectivity data (with a time resolution of 10 min) were interpolated to a Cartesian grid using the National Center for Atmospheric Research REORDER software. A grid spacing of 0.75 km in the horizontal and 0.5 km in the vertical was adopted with the grid origin fixed at the nominal position of the R/V *Vickers.* Reflectivity images at a constant altitude of 1 km were used in this study to monitor and classify convective activity and to calculate rain rates.

The IMET buoy was located near 1°45′S, 156°E. Table 1 provides a summary of the instrumentation mounted on the IMET buoy. Weller and Anderson (1996) provided a complete description of the IMET deployment, including data collection procedures, instrument accuracy, and postdeployment data processing procedures. Surface meteorological data with a time resolution of 7.5 min were used for the current study. The air temperature, SST, relative humidity, and barometric pressure were each sampled for 2.5 s once within the 7.5-min time interval, whereas the shortwave and longwave radiation values were averaged over the entire 7.5-min period. The wind velocity was a vector average over that same time interval (Weller and Anderson 1996).

b. Classification of convective organization

The convective classification scheme developed by Rickenbach and Rutledge (1998) was based on the spatial scale and horizontal morphology of radar reflectivity images. Systems were classified as MCS scale if the spatial scale of the contiguous radar echo was greater than 100 km (Houze 1993); otherwise the systems were classified as sub-MCS scale. The systems were also classified as being linearly organized if the convective elements were aligned in a linear fashion during the period when they were observed by radar and nonlinear if they exhibited no obvious linear characteristics. Rickenbach and Rutledge found that the two dominant modes of convective organization were sub-MCS-scale nonlinear systems and MCS-scale linear systems. Combined, these two classifications accounted for over 90% of the rainfall and were observed about 90% of the time during the period of COARE shipboard radar observations. A brief overview of these two types of convective organization will be given below.

Convective systems whose contiguous radar echoes had a spatial scale less than 100 km and exhibited no linear organization while being observed by radar were classified as sub-MCS-scale nonlinear events (SM-NL; Fig. 1a). These systems were the most frequently observed type of convective organization, being present nearly half of the time. However, because of the their limited spatial scale, they produced a small, but nonnegligible portion (13%) of the total rainfall observed within the radar coverage area during COARE. These systems were most prolific during very light wind periods. However, they were also observed during 2–3-day periods following westerly wind burst maxima (Rickenbach and Rutledge 1998).

Convective systems whose contiguous radar echoes had a spatial scale greater than 100 km and exhibited linear organization were classified as MCS-scale linear events. These events were present over 40% of the time and produced approximately 80% of the total rainfall observed within the radar coverage area. They were deemed to be more common during westerly wind burst periods, but they were observed in all wind regimes (Rickenbach and Rutledge 1998). A significant trailing stratiform precipitation region was also generally as-

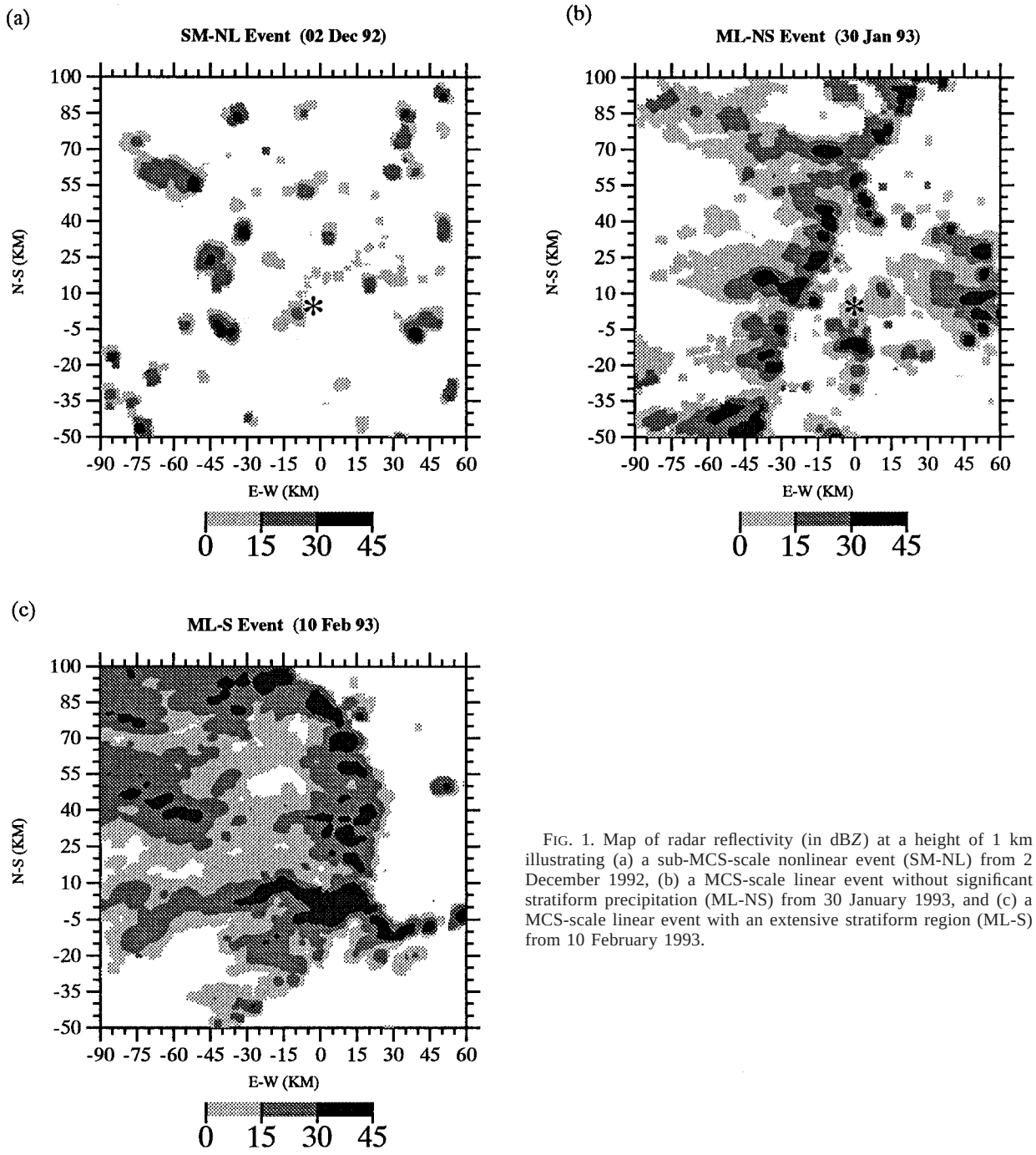

FIG. 1. Map of radar reflectivity (in dBZ) at a height of 1 km illustrating (a) a sub-MCS-scale nonlinear event (SM-NL) from 2 December 1992, (b) a MCS-scale linear event without significant stratiform precipitation (ML-NS) from 30 January 1993, and (c) a MCS-scale linear event with an extensive stratiform region (ML-S) from 10 February 1993.

sociated with these events, however, this was not always the case. Since the presence of significant stratiform precipitation will affect boundary layer recovery (Zipser 1977), we further subdivided this classification based on the presence of stratiform precipitation. The presence of a trailing stratiform precipitation region provides an indication that the system had reached a mature stage (i.e., had mesoscale flow features associated with it). Systems without a significant trailing stratiform region were usually in a developing stage. Figure 1b shows an example of a MCS-scale linear event without significant trailing stratiform precipitation (ML-NS), and Fig. 1c shows an example of a MCS-scale linear event with extensive trailing stratiform precipitation (ML-S).

c. Calculation of surface fluxes

The surface meteorological data collected by the IMET buoy were used to calculate the wind stress along with the sensible and latent heat fluxes. An updated version (version 2.5a) of the COARE bulk flux algorithm described in Fairall et al. (1996b) was used to calculate surface fluxes. The COARE algorithm is an extension of the Liu-Katsaros-Businger Model described by Liu et al. (1979). In the COARE algorithm, a gustiness velocity is calculated and added to the measured wind speed to account for free convection and wind gustiness. The COARE algorithm also includes a warm layer and cool skin model to obtain an improved estimate of the interfacial SST (Fairall et al. 1996a).

The rain rates were calculated using reflectivity data from the MIT radar. This allowed the evolving structure of the precipitation in the vicinity of the IMET buoy to be closely monitored. The radar-derived rain rates in a 4.5-km box surrounding the nominal position of the IMET buoy were used in this study. A domain of this size was chosen to account for uncertainties in the recorded positions of both the R/V *Vickers* and the IMET buoy. The uncertainties in the location of the R/V *Vickers* were on the order of 1 km and the IMET buoy had a watch radius of 1.276 km (M. Baumgardener 1996, personal communication).

The methods used to derive rain rates from radar reflectivity fields are similar to the methods described in Rickenbach and Rutledge (1998), so only a brief overview will be given here. Reflectivity values were interpolated to a Cartesian grid and partitioned into convective and nonconvective components. A first guess rain rate was calculated with respective *Z–R* relations using the partitioned reflectivity data. The convective/nonconvective partitioning algorithm was based on the methodology of Steiner and Houze (1993) and Steiner et al. (1995). The *Z–R* relations were taken from Tokay and Short (1996), who derived these relations based on surface disdrometer observations from Kapingamarangi Atoll during TOGA COARE. The rain-rate field was then corrected for attenuation (following Patterson et al. 1979) and converted back to reflectivity by inverting the same *Z–R* relations. The attenuation-corrected reflectivity field was then repartitioned into convective and nonconvective components. The final rain rate was then obtained by applying the respective *Z–R* relations to the newly partitioned reflectivity field.

Rainfall in the Tropics typically has a sensible heat flux associated with it since the temperature of the falling precipitation, which is approximately at the environmental wet-bulb temperature (Kinzer and Gunn 1951), is less than the SST. The effects of cold precipitation falling on a warm ocean is of particular interest to the oceanographic community since during heavy rain events, it can result in significant changes in the SST (Price 1979; Tomczak 1995; Flament and Sawyer 1995). The heat flux associated with rainfall (Q_{RF}) was calculated using the methods described by Gosnell et al. (1995):

$$Q_{RF} = 2.6R\Delta T, \quad (1)$$

where R is the rain rate in mm h^{-1} and ΔT is the air–sea temperature difference. The average rain rate within a 4.5-km box surrounding the nominal position of the IMET buoy was used to calculate the rainfall heat flux.

3. Composite analyses

a. Compositing procedure

Convective systems are known to drastically affect the atmospheric boundary layer. The outflows created by convection have been associated with significant decreases in air temperature and increases in wind speed (Addis et al. 1984). In the wake of convective events the air temperature generally increases, approaching its undisturbed environmental value. This study made a special effort to separate the convectively active phase from the recovery phase in the compositing process. In this way, distinct processes occurring in the two phases will not be mixed in the final composites, thereby leading to a more accurate representation of the boundary layer's response to the convective system.

The compositing scheme employed consists of four sections that represent the preconvective, convectively active, recovery, and postrecovery time periods. The start of the convectively active period was designated when the air temperature began to decrease in response to convective activity (a temperature drop of at least 1°C was required). The convectively active phase ended, and the start of the recovery phase was indicated, once the minimum air temperature and maximum wind speed were both observed. Because three bins were used in the convectively active phase and rain rates were sampled every 10 min, the convectively active phase was required to be at least 30 min in duration. The end of the recovery phase was reached when the 2-h running mean air temperature started to decrease and continued to decrease for eight consecutive 7.5-min time periods (i.e., 1 h). This warming reversal criteria, which was similar to the approach employed by Young et al. (1995), indicated that other processes, such as advection or the presence of an adjacent convective system, were playing significant roles in modifying the boundary layer air temperature. Once the convectively active and recovery phases were designated for each individual event, they were separated into three and five equally spaced (with respect to time) sections (or bins), respectively, and the variables were averaged over those time periods. Preconvective and postrecovery bins were included prior to and after the convectively active and recovery phases, respectively. These bins were defined to be 1 h in length for each class of convective organization. Hence, each composite time series has a total of 10 bins. The preconvective bin described the envi-

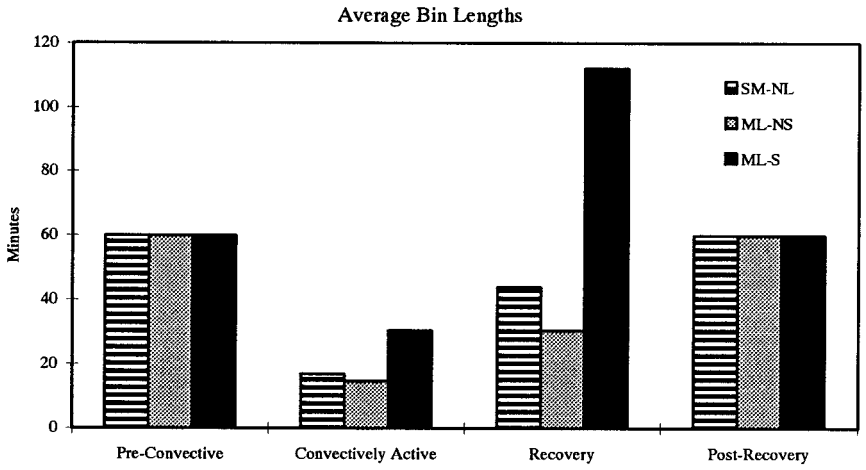

FIG. 2. Average bin lengths (in minutes) during the preconvective, convectively active, recovery, and postrecovery phases for the SM-NL, ML-NS, and ML-S classifications of convective organization.

ronmental conditions prior to convective activity and helped illustrate the changes induced by the convective system. The postrecovery bin was useful in checking the accuracy of the recovery termination criteria.

For the current study, 29 individual time series were developed and used to produce composite time series of wind stress, latent heat flux, sensible heat flux, and sensible heat flux associated with rainfall for each class of convective organization. Composites of the pertinent bulk atmospheric and oceanic variables were also produced to illustrate the conditions responsible for the surface flux enhancements. Of the 29 individual convective events (as identified by radar) that were used to produce the composites; nine were SM-NL events, nine were ML-NS events, and eleven were ML-S events.

Since the different classifications of convective organization discussed in section 2b have dissimilar spatial and temporal scales, the bins representing the convectively active and recovery periods had different lengths in the composites. This was beneficial in the sense that convective and recovery processes work on different timescales. Within convectively active regions, the conditions change very rapidly, whereas in recovery regions, the conditions change much more slowly. The separation of the two regimes allowed for different bin lengths, which better represent the physical processes occurring within these periods. Figure 2 summarizes the average bin lengths for the preconvective, convectively active, recovery, and postrecovery bins for the three types of convective organization.

For the SM-NL and ML-NS events, the average length of each convectively active bin was relatively short at 16.9 and 14.7 min, respectively, whereas for the ML-S events they were significantly longer at 30.5 min. The recovery bins were over twice as long as the convectively active bins for each respective type of convective organization. For the SM-NL and ML-NS events, the average recovery bin length was 43.8 and 30.5 min, respectively, whereas for the ML-S events, the average recovery bin length was nearly three times as long, at 112.1 min. The main reason the recovery time for the ML-S events was much longer than for the other classifications was that this convective classification typically induced larger temperature depressions. Furthermore, because of the significant stratiform precipitation component, the rate at which the boundary layer air temperature could recover to the preconvective value was reduced. The average bin lengths for the preconvective, convectively active, recovery, and post recovery bins shown in Fig. 2 have been used to convert the composites back to time series format. The resulting composite time series are presented in the following sections.

b. Rainfall

Figure 3 depicts the composite time series of rain rates for each of the three types of convective organization identified in this study. Mean rain rates computed within a 4.5 km $\times$ 4.5 km box surrounding the IMET buoy were used to produce these composites. As expected, the largest rain rates were observed during the convectively active phase for each type of convective organization. The ML-S composite exhibit the largest mean rain rate (7 mm h^{-1}), whereas the SM-NL and ML-NS composites show peak mean rain rates of 4.5 mm h^{-1} and 3 mm h^{-1}, respectively. This implies that the ML-S events produced more intense rainfall rates compared to the other two types of convective organization.

In the ML-S composites, the first one or two recovery bins also showed appreciable rain rates (0.2 mm h^{-1} to 1 mm h^{-1}) associated with nonconvective (stratiform) precipitation. The SM-NL composite exhibited similar behavior, caused primarily by the fact that these events

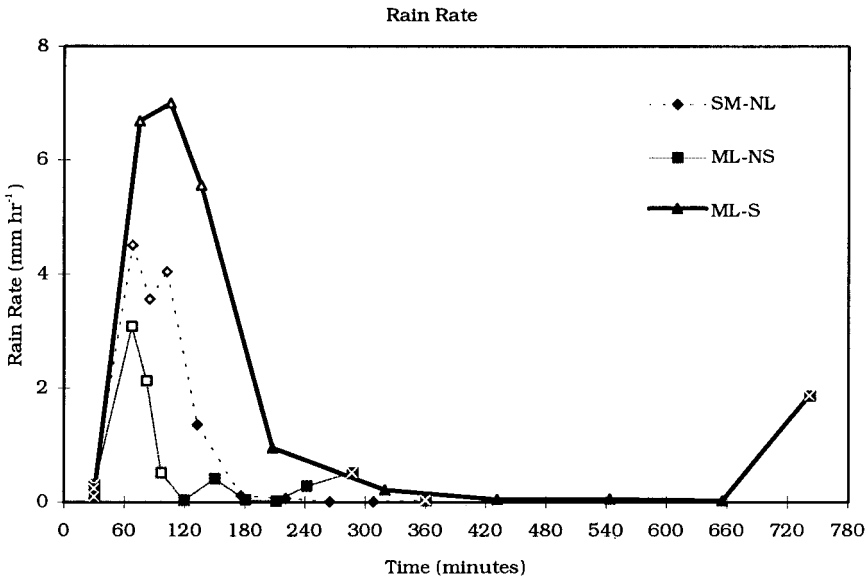

FIG. 3. Composite time series of mean radar-derived rain rate within a 4.5 km × 4.5 km box centered over the nominal location of the IMET buoy. Open markers represent convectively active bins and filled markers represent recovery bins. Squares with crosses represent preconvective and postrecovery periods. Time was calculated using the average bin lengths given in Fig. 2.

had very little motion associated with them and a portion of the precipitating cell was still within the 4.5 km × 4.5 km box when the boundary layer recovery began. Since the separation into convectively active and recovery time periods was based solely on air temperature and wind speed, the fact that the rain rates decreased significantly between the two periods supports the rationale employed to distinguish between these two periods. The postrecovery bins also showed significant rain rates due to the presence of new precipitating systems, which often triggered the recovery termination criteria.

c. Wind stress

The wind stress is important for air–sea interaction because it results in the transfer of kinetic energy to the upper ocean. This kinetic energy aids in driving surface currents and the production of turbulence, which controls the depth of the oceanic mixed layer (Pickard and Emery 1990). In a bulk aerodynamic formulation, the wind stress is proportional to the product of the wind speed squared and the drag coefficient. The drag coefficient is a function of the surface-layer stability and the surface roughness, which is also a function of the wind speed. Therefore, the wind stress is extremely sensitive to changes in wind speed and it would be expected that the enhanced winds associated with convective scale downdrafts would lead to greatly enhanced wind stress values.

Figure 4a shows the composite wind speed response to the three types of convective organization with each exhibiting significant enhancements in the surface wind speed during the convectively active phase. In the SM-NL composite, the average peak wind speed during the convectively active phase was approximately 4 m s^{-1}, an increase of approximately 2 m s^{-1} from the preconvective environment. The MCS-scale linear composites exhibited an increase of about 3 m s^{-1} from the preconvective conditions with average peak wind speeds of about 7 m s^{-1} and 9 m s^{-1} for the ML-NS and ML-S events, respectively, during the convectively active phase. Wind speeds decreased significantly during the recovery phase and were approximately equal to or slightly greater than the preconvective conditions in the SM-NL and ML-NS composites. For the ML-S events, the wind speeds were actually weaker than the preconvective value during the later part of the recovery. A similar wind speed minima was observed for a GATE squall line by Gamache and Houze (1982).

Young et al. (1995) hypothesized that the wind speed enhancements due to active convection were independent of the preconvective environment. The results of the current study do not necessarily discount this hypothesis, but they do indicate that the wind speed enhancements are quite sensitive to the organizational modes of the active convection causing the enhancement, which are in turn related to the preconvective conditions through ambient shear and instability (Betts et al. 1976; Barnes and Sieckman 1984; Rotunno et al. 1988).

The composite surface wind stress response to the three types of convective organization is shown in Fig. 4b. The shape of the wind stress composite is very similar to the wind speed composite, as expected. The variations in the drag coefficient (not shown) are small com-

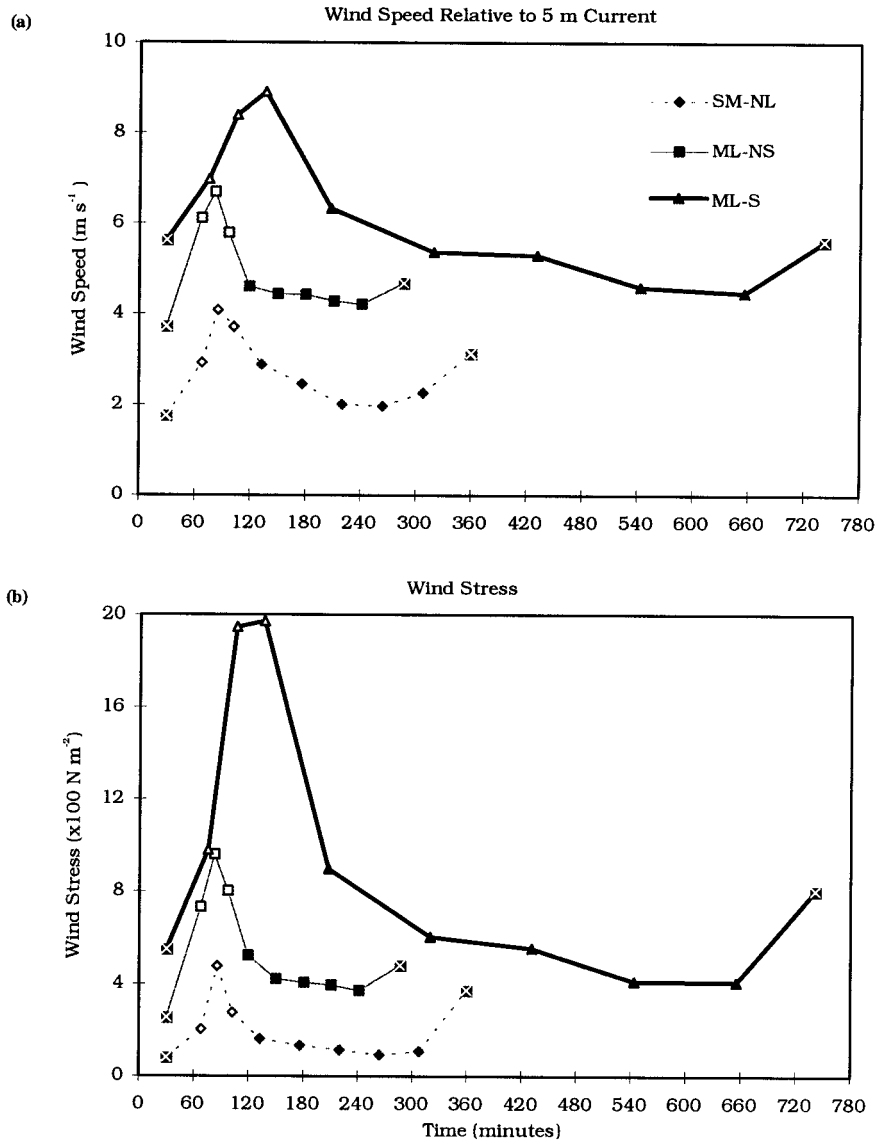

FIG. 4. Same as Fig. 3 except for (a) wind speed relative to the 5-m current and (b) wind stress.

pared to the variations in wind speed. The largest enhancements occurred during the convectively active phase for all modes of convective organization. The composite for the ML-S events showed the greatest enhancements (increasing from about 0.05 N m^{-2} to nearly 0.2 N m^{-2}). The wind stress enhancements for the other two types of convective organization were much smaller, increasing from about 0.02 N m^{-2} to 0.1 N m^{-2} and from about 0.01 N m^{-2} to 0.05 N m^{-2} in the ML-NS and SM-NL composites, respectively. During the recovery, the wind stress values were similar to the preconvective values.

d. Sensible heat flux

The sensible heat flux is controlled primarily by the wind speed and the air–sea temperature difference. Since convective-scale downdrafts are cool relative to the ocean surface, the sensible heat flux should be significantly enhanced in regions of active convection. The sensible heat flux also remains enhanced during the boundary layer recovery as a finite amount of time is required for the air temperature to recover to its preconvective value. Any precipitation during the recovery will lead to a longer period of enhanced sensible heat flux because the surface air temperature will tend to remain depressed due to evaporational cooling below cloud base.

The composite air–sea temperature difference response to the three types of convective organization is shown in Fig. 5a. The SST changes were relatively small (Fig. 5b), and therefore the air–sea temperature difference response was dominated by changes in the surface

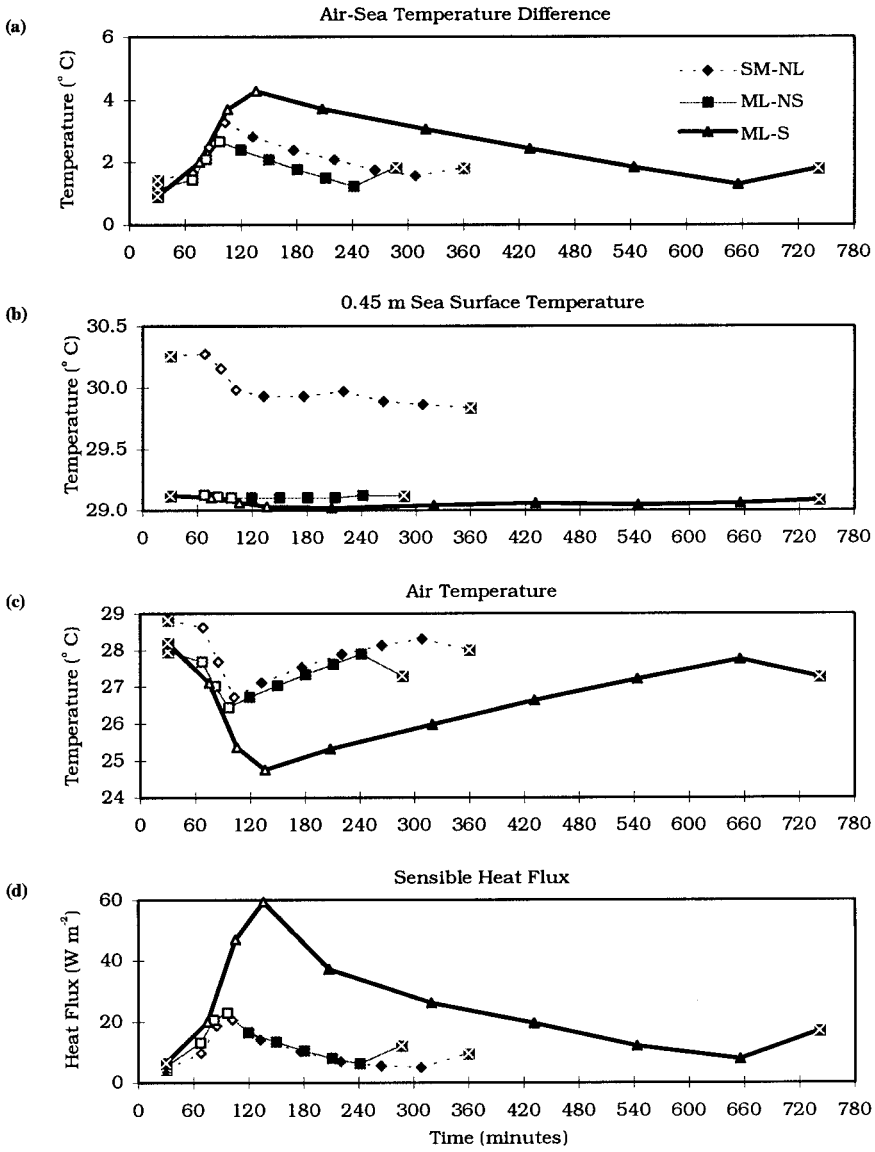

FIG. 5. Same as Fig. 3 except for (a) air–sea temperature difference, (b) SST at a depth of 0.45 m, (c) air temperature, and (d) sensible heat flux.

air temperature (Fig. 5c). The SM-NL and ML-NS composites show the smallest air temperature depressions (about 2° and 1.5°C, respectively) during the convectively active phase, which lead to an increase in the air–sea temperature difference by about the same amount. Conversely, the air–sea temperature difference increased by about 3.5° C in the ML-S composite. This behavior is consistent with Barnes and Garstang (1982), who found that air temperature depressions increased with increasing rain rates. During the recovery phase the air–sea temperature difference decreased to approximately the preconvective environmental value. The rate at which the air–sea temperature decreased was approximately the same in the SM-NL and ML-NS composites. The air–sea temperature difference decreased at a slower rate in the ML-S composite, however, most likely due to the presence of stratiform precipitation and extensive cloud cover reducing the incoming solar radiation.

In the SM-NL composite of SST, the preconvective SST was about 1°C warmer than for the other types of convective organization and the composite SST decreased by about 0.4°C. SM-NL events tended to develop during periods of weak winds and limited cloud cover (Rickenbach and Rutledge 1998), leading to the formation of a near-surface diurnal warm layer, which is typically on the order of meters deep (Bruce and Firing 1974; Price et al. 1986; Lukas 1991). This diurnal warm layer may also play an important role in the development of SM-NL events in the late afternoon, when

the warm layer was well developed and the SST was maximum. During periods when this warm layer is present, the ocean is much more responsive to atmospheric forcing than during periods when the warm layer is absent and the oceanic mixed layer is much deeper. This allows the weak forcing associated with the SM-NL events to cause much larger SST changes than the stronger forcing associated with the other types of convective organization. The cause of the SST decrease associated with the SM-NL events is probably enhanced mixing associated with the increased wind speeds (i.e., warmer water near the surface being mixed with cooler water below). This process would initially cause a warming at the 0.45-m depth as indicated by the first convective bin.

The composite sensible heat flux response to the three types of convective organization is shown in Fig. 5d. The preconvective sensible heat flux values were approximately 5 W m^{-2} for all types of convective organization. During the convectively active phase the sensible heat flux increased significantly for all types of convective organization. The SM-NL and ML-NS composites are nearly identical, with sensible heat flux values increasing from about 5 W m^{-2} to about 20 W m^{-2} during the convectively active phase. The enhancements depicted in the ML-S composites were much larger, increasing from about 5 W m^{-2} to nearly 60 W m^{-2}. During the recovery phase, the sensible heat flux decreased with time to nearly the preconvective value for all types of convective organization, determined largely by the rate at which the surface air temperature recovered to the preconvective environmental value.

e. Latent heat flux

The latent heat flux is controlled primarily by the wind speed and the air–sea humidity difference. Figure 6a shows the composite air–sea humidity difference response to the three types of convective organization. In the SM-NL composite, changes in the saturation specific humidity at the SST (Fig. 6b) are primarily responsible for the observed air–sea humidity difference, which decreases throughout the composite time series. For the other two types of convective organization, changes in the specific humidity (Fig. 6c) are largely responsible for the observed air–sea humidity difference changes, as the saturation specific humidity at the SST is nearly constant. In the ML-NS composite, the air–sea humidity difference increased by only about 0.5 g kg^{-1} during the last part of the convectively active and at the very beginning of the recovery phases. In the ML-S composites, the air–sea humidity difference increased by nearly 1.5 g kg^{-1} during the convectively active phase and remained enhanced by about 1 g kg^{-1} for over half of the recovery phase. The larger enhancement of the air–sea humidity differences for the MCS-scale events may be linked to the presence of relatively dry mesoscale downdrafts below the associated stratiform precipitation. The presence of mesoscale downdrafts have not been explicitly demonstrated in this study; however, their presence would be expected based on previous studies (Zipser 1977; Gamache and Houze 1982). It should be noted that while the minimum specific humidity is not depicted in the recovery period of the ML-S composite as would be expected (Zipser 1977; Gamache and Houze 1982; Johnson and Nicholls 1983), nearly all of the individual time series had either absolute or relative minimum specific humidity values sometime during the recovery phase. However, this signal was smoothed in the compositing process, with only a weak relative minimum being depicted in the second recovery bin.

The composite latent heat flux response to the three types of convective organization is shown in Fig. 6d. For all types of convective organization the latent heat flux approximately doubled during the convectively active phase. During the recovery, the latent heat flux decreased significantly as the wind speed subsided. However, the latent heat flux remained slightly enhanced (by between 25% and 50% from the preconvective environment) during the first few recovery bins for the ML-S events. This is consistent with Johnson and Nicholls (1983), who observed latent heat flux enhancements in the wake of an intense GATE squall line. The modeling study of Trier et al. (1996) also produced significantly enhanced latent heat fluxes under the stratiform region in a COARE squall line simulation.

f. Heat flux associated with rainfall

Figure 7 shows the composite sensible heat flux associated with rainfall for the three types of convective organization. In each case the heat flux associated with rainfall peaked during the convectively active phase since rain rates and air–sea temperature differences both peaked during this period. The rainfall heat flux peak in the ML-S composite (about 75 W m^{-2}) was over twice that of the other two types of convective organization. This is not unexpected, especially considering that the method of Gosnell et al. (1995) [which relates the rainfall heat flux to the rain rate and the air–sea temperature difference] was used to calculate this heat flux and the ML-S events produced both the largest mean rain rates (section 3b) and the greatest air–sea temperature differences (section 3d). Note however, that the resultant smaller rainfall heat fluxes were still approximately equal to the corresponding sensible heat flux and therefore may be of importance for certain oceanic mixed layer modeling activities. The rainfall heat flux values during the recovery were greatly reduced due mainly to smaller rain rates. The large rainfall heat flux values depicted by the postrecovery bins were due to the occurrence of other precipitating systems that often triggered the recovery termination criteria. The peak rainfall heat flux values are consistent with the results of Gosnell et al. (1995) and Flament and Sawyer

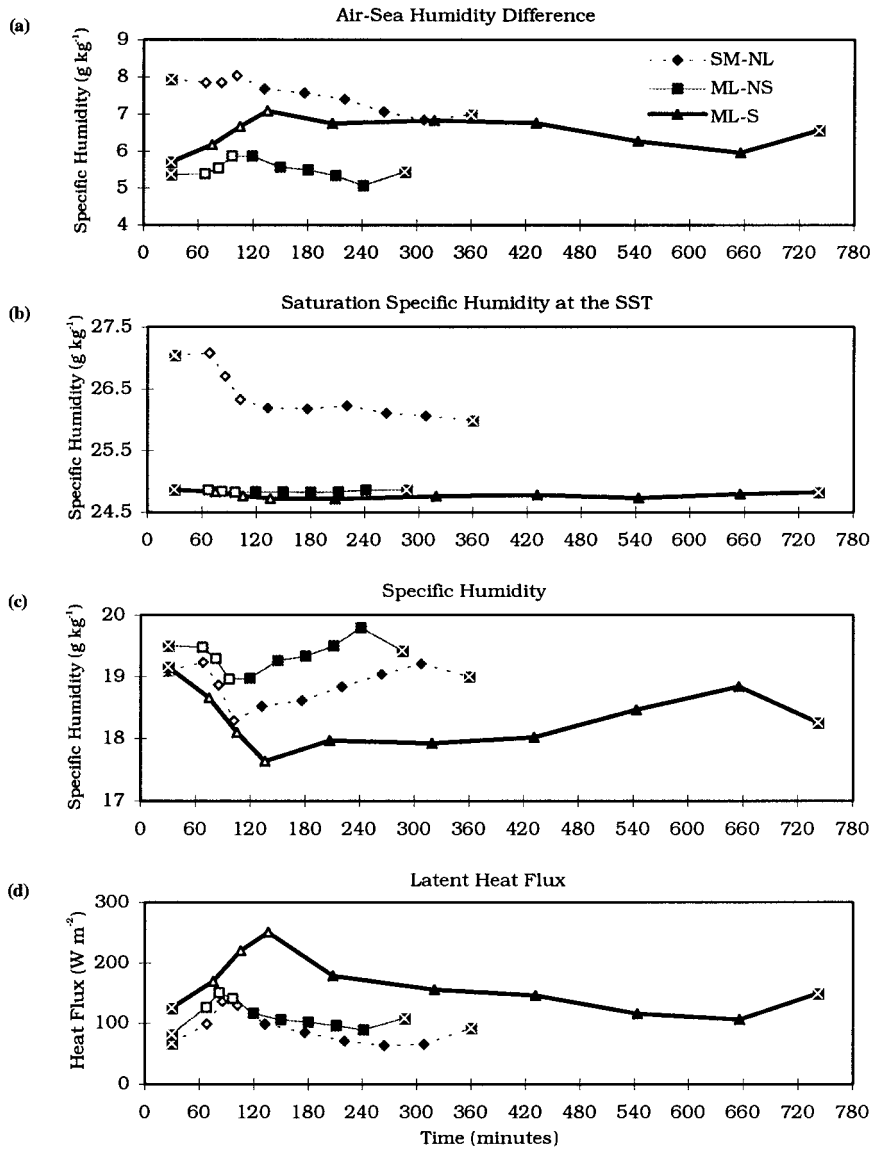

FIG. 6. Same as Fig. 3 except for (a) air–sea humidity difference, (b) saturation specific humidity at the SST, (c) specific humidity, and (d) latent heat flux.

(1995), who observed rainfall heat flux values in excess of 100 W m^{-2} during intense convective activity.

g. Evaluation of composites

To evaluate how well the composite time series represent individual cases, a correlation analysis was performed. The average correlation coefficient for every variable discussed above was calculated for each type of convective organization. The results of this analysis are summarized in Table 2. The correlation coefficients for this study generally range from 0.5 to 0.9, with many values greater than 0.6. A similar analysis was done by Young et al. (1995) and the correlation coefficients obtained in the present study are higher for nearly every category, thereby suggesting that the composites produced in the current study provide an improved representation of the surface flux response to atmospheric convection over the western Pacific warm pool. These improvements can be attributed to the use of a classification scheme that differentiated between different types of convective organization and to the use of a more sophisticated compositing scheme that differentiated between the convectively active and recovery portions of the individual events. This compositing scheme allowed for the use of two separate temporal scales, thereby allowing the response to convective and recovery processes to both be well represented in the final composite analyses.

The results of this study can be further evaluated by

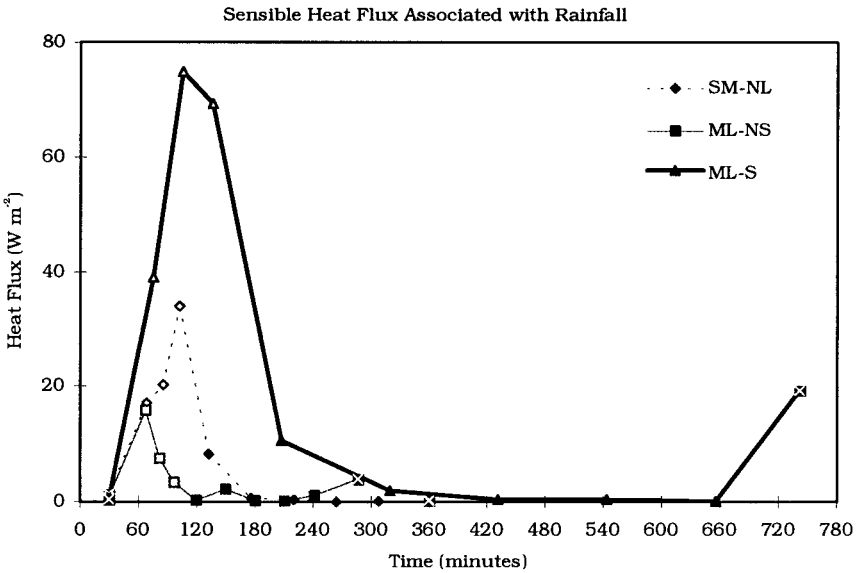

FIG. 7. Same as Fig. 3 except for sensible heat flux associated with rainfall.

comparing them to findings from previous studies. Since previous studies typically focused on MCS-scale systems (primarily squall lines), only the composite results for the ML-S classification will be considered for this comparison. Table 3 summarizes the results for the ML-S composites produced in the current study along with the results from four previous studies. The Johnson and Nicholls (1983) study was a composite analysis of an intense squall line observed during GATE, Addis et al. (1984) analyzed 49 GATE gust fronts, Young et al. (1995) was a composite analysis from TOGA COARE, and Jabouille et al. (1996) was a TOGA COARE based modeling study of two linear MCSs. The results of the present study are basically in agreement with all of these previous studies, which is encouraging since other composite analyses, an individual event from GATE, and a model result are all represented in the table. It should be noted that the environmental conditions, namely vertical wind shear and static stability, in GATE were different than those in the COARE region and the methods used to compute the surface fluxes were also different. The analysis of Young et al. (1995) was done to document the evolution of convective wakes during TOGA COARE and in doing so they used hourly averaged data in equally spaced bins. This practice effectively smoothed out the response during the convectively active period. Hence, larger magnitude responses are evident in the present study. The results of the present study compare favorably to those for individual squall lines reported by Johnson and Nicholls (1983) and Jabouille et al. (1996). The surface responses reported by Johnson and Nicholls are somewhat larger in magnitude than those found in the current study. This result is not unexpected considering that Johnson and Nicholls reported on an individual case whereas the present study describes the average response based on a large number of cases.

TABLE 2. Summary of mean correlation coefficients between the individual cases and the composite time series. Values given are the mean correlation coefficients (r) for the sub-MCS-scale nonlinear (SM-NL), MCS-scale linear with no significant stratiform precipitation region (ML-NS), and MCS-scale linear with significant stratiform precipitation (ML-S) events.

Variable	SM-NL	ML-NS	ML-S
Relative wind speed	0.58	0.64	0.60
Drag coefficient	0.37	0.33	0.62
Wind stress	0.50	0.61	0.59
Sensible heat flux	0.79	0.75	0.81
Air temperature	0.91	0.78	0.86
Sea surface temperature	0.71	0.20	0.53
Transfer coefficient for heat	0.46	0.38	0.39
Latent heat flux	0.67	0.64	0.62
Specific humidity	0.54	0.52	0.66
Surface saturation specific humidity	0.70	0.15	0.46
Transfer coefficient for moisture	0.46	0.40	0.39
Rate of air temperature change	0.87	0.77	0.81
Air–sea humidity difference	0.53	0.50	0.60
Air–sea temperature difference	0.86	0.78	0.86
Mean rain rate	0.61	0.59	0.66
Rainfall heat flux	0.56	0.52	0.66

4. Decomposition of sensible and latent heat fluxes

a. Decomposition methods

When bulk aerodynamic formulas are used to determine sensible and latent heat fluxes, variations in the respective bulk variables and transfer coefficients lead to variations in the respective heat flux. To develop parameterizations to account for sub-grid-scale sensible and latent heat flux enhancements associated with convective activity, the processes responsible for the en-

TABLE 3. Comparison of results for the MSC-scale linear with stratiform precipitation composites (ML-S) to previous studies that examined similar types of events. Values given are maximum or minimum values during the convectively active period and the values in parentheses are the maximum change from the preconvective environment. The studies shown are Johnson and Nicholls (1983) (JN83), Addis et al. (1984) (A84), Young et al. (1995) (Y95), and Jabouille et al. (1996) (J96).

Variable	ML-S	JN83	A84	Y95	J96
Max. wind, speed (m s^{-1})	8.9 (3.3)	15 (10)	7.7 (2.6)	6 (1)	11 (8)
Max. wind stress (N m^{-2})	0.2 (0.15)	—	—	0.08 (0.02)	—
Min. air temperature (°C)	24.8 (−3.4)	22 (−4)	24.2 (−1.9)	26 (−1.5)	24 (−3)
Max. air–sea temperature difference (°C)	4.3 (3.4)	—	—	3 (1.5)	—
Max. sensible heat flux (W m^{-2})	59 (52)	100 (80)	78 (63)	35 (20)	70 (60)
Min. specific humidity (g kg^{-1})	17.6 (−1.6)	13.5 (−2.5)	16.7 (−0.1)	18.5 (−0.5)	18.2 (−1)
Max. air–sea humidity difference (g kg^{-1})	7.1 (1.4)	—	—	6 (0.2)	—
Max. latent heat flux (W m^{-2})	250 (125)	400 (300)	356 (175)	155 (50)	275 (175)
Peak mean rain rate (mm h^{-1})	7	—	—	7.5	—
Max. rainfall heat flux (W m^{-2})	75	—	—	40	—
Description of study	TOGA COARE composite	Intense GATE squall line	Average of 49 GATE gust fronts	TOGA COARE composite	TOGA COARE modeling study

hancements need to be identified. Previous studies have shown that convective activity leads to significantly cooler and somewhat drier conditions at the surface and produce greatly enhanced wind speeds (Barnes and Garstang 1982; Johnson and Nicholls 1983; Addis et al. 1984; Young et al. 1995). However, the relative importance of these changes as a function of convective organization has not been determined.

In order to examine the various contributions (e.g., wind speed, air–sea temperature difference, air–sea humidity difference, etc.) to the sensible and latent heat flux enhancements, a perturbation analysis was carried out on the bulk formulas for the sensible (Q_{SH}) and latent (Q_{LH}) heat fluxes:

$$Q_{SH} = \rho_a c_p |U| \Delta T C_T, \tag{2a}$$

$$Q_{LH} = \rho_a L_e |U| \Delta q C_E. \tag{2b}$$

The wind speed ($|U|$), air–sea temperature (ΔT) and humidity (Δq) differences, and the transfer coefficients for heat (C_T) and moisture (C_E) were broken into a preconvective value component ($\tilde{X}$) plus a perturbation from the preconvective value component (X') (i.e., $X = \tilde{X} + X'$). Upon substitution into (2a) and (2b), the following relations were obtained for the enhancements of the sensible and latent heat fluxes:

$$\begin{aligned} Q_{SH} - \rho_a c_p |\tilde{U}| \Delta \tilde{T} \tilde{C}_T &= \rho_a c_p (\underbrace{|U|' \Delta \tilde{T} \tilde{C}_T}_{\text{(i)}} + \underbrace{|\tilde{U}| \Delta T' \tilde{C}_T}_{\text{(ii)}} + \underbrace{|\tilde{U}| \Delta \tilde{T} C'_T}_{\text{(iii)}} \\ &\quad + \underbrace{|U|' \Delta T' \tilde{C}_T}_{\text{(iv)}} + \underbrace{|\tilde{U}| \Delta T' C'_T}_{\text{(v)}} + \underbrace{|U|' \Delta \tilde{T} C'_T}_{\text{(vi)}} \\ &\quad + \underbrace{|U|' \Delta T' C'_T}_{\text{(vii)}}), \end{aligned} \tag{3a}$$

$$\begin{aligned} Q_{LH} - \rho_a L_e |\tilde{U}| \Delta \tilde{q} \tilde{C}_E &= \rho_a L_e (\underbrace{|U|' \Delta \tilde{q} \tilde{C}_E}_{\text{(i)}} + \underbrace{|\tilde{U}| \Delta q' \tilde{C}_E}_{\text{(ii)}} + \underbrace{|\tilde{U}| \Delta \tilde{q} C'_E}_{\text{(iii)}} \\ &\quad + \underbrace{|U|' \Delta q' \tilde{C}_E}_{\text{(iv)}} + \underbrace{|\tilde{U}| \Delta q' C'_E}_{\text{(v)}} + \underbrace{|U|' \Delta \tilde{q} C'_E}_{\text{(vi)}} \\ &\quad + \underbrace{|U|' \Delta q' C'_E}_{\text{(vii)}}). \end{aligned} \tag{3b}$$

The first three terms on the right-hand side represent the components associated with perturbations in wind speed, air–sea temperature or humidity differences, and transfer coefficients, respectively. The last four terms account for nonlinear effects associated with simultaneous variations between the bulk variables or between the bulk variables and the respective transfer coefficients.

b. Sensible heat flux enhancements

Table 4 shows the total sensible heat flux enhancements along with its decomposition into the seven terms on the right-hand side of (3a). The contributions by terms i, ii, and iv (which represent variations in wind speed, air–sea temperature difference, and the simultaneous variations of these two variables, respectively) are the most significant for all three types of convective organization. This finding is consistent with previous studies by Ledvina et al. (1993) and Jabouille et al. (1996), despite the use of a different methodology.

For the SM-NL and ML-NS events, terms i, ii, and iv contribute approximately the same amount to the total enhancement during the convectively active phase, while term ii was the primary contributor during the recovery since significant wind speed enhancements were confined to the convectively active phase and the

TABLE 4. The decomposition of the sensible heat flux enhancements into the individual terms on the right-hand side of Eq. (3a). The individual enhancements for (a) SM-NL, (b) ML-NS, and (c) ML-S composites, along with their total enhancements (TE), are shown for the three convectively active (CA) and five recovery (REC) bins. Values shown are in W m^{-2}, with positive values indicating an enhancement of the upward-directed heat flux.

Period	Term i	Term ii	Term iii	Term iv	Term v	Term vi	Term vii	TE_{SH}
				(a) SM-NL				
CA1	2.94	0.66	−0.24	0.44	−0.04	−0.16	−0.02	3.58
CA2	5.86	3.19	−0.48	4.24	−0.35	−0.64	−0.46	11.36
CA3	4.91	5.65	−0.58	6.30	−0.74	−0.64	−0.82	14.08
REC1	2.84	4.26	−0.50	2.75	−0.48	−0.32	−0.31	8.23
REC2	1.77	2.94	−0.42	1.19	−0.28	−0.17	−0.11	4.92
REC3	0.64	1.97	0.01	0.29	0.01	0.00	0.00	2.92
REC4	0.54	0.97	−0.12	0.12	−0.03	−0.01	0.00	1.47
REC5	1.30	0.39	−0.38	0.12	−0.03	−0.11	−0.01	1.27
				(b) ML-NS				
CA1	3.44	1.29	−0.02	0.83	0.00	−0.01	0.00	5.53
CA2	4.27	4.32	0.13	3.46	0.10	0.10	0.08	12.47
CA3	2.98	6.99	0.14	3.90	0.19	0.08	0.10	14.38
REC1	1.28	5.72	0.18	1.37	0.19	0.04	0.05	8.82
REC2	1.03	4.27	0.11	0.82	0.09	0.02	0.02	6.36
REC3	1.02	2.81	0.05	0.54	0.03	0.01	0.00	4.46
REC4	0.80	1.57	0.09	0.24	0.03	0.01	0.00	2.75
REC5	0.71	0.31	0.04	0.04	0.00	0.01	0.00	1.12
				(c) ML-S				
CA1	1.56	7.82	0.36	1.88	0.44	0.09	0.10	12.26
CA2	3.21	19.90	0.65	9.79	1.98	0.32	0.97	36.82
CA3	3.81	24.07	0.62	14.06	2.29	0.36	1.34	46.54
REC1	0.81	20.02	0.52	2.48	1.59	0.06	0.20	25.68
REC2	−0.31	15.39	0.45	−0.72	1.06	−0.02	−0.05	15.79
REC3	−0.38	10.85	0.22	−0.64	0.37	−0.01	−0.02	10.38
REC4	−1.20	6.55	0.14	−1.21	0.14	−0.03	−0.03	4.37
REC5	−1.35	2.74	0.38	−0.57	0.16	−0.08	−0.03	1.25

air–sea temperature difference was enhanced during all periods (consistent with Jabouille et al. 1996). For the ML-S events, term ii was the primary contributor during the convectively active periods, followed by terms iv and i in decreasing order of significance. This is due to that fact that the ML-S events produced much greater air temperature depressions (and hence greater air–sea temperature differences) than the other event types. During the recovery, term ii was the primary contributor, again because the significant wind speed enhancements were confined to the convectively active phase.

The partitioned enhancement in heat transfer from the ocean to the atmosphere via sensible heat fluxes during the convectively active and recovery phases is summarized in Table 5. These enhancements were calculated using the sensible heat flux enhancements provided in Table 4 with the average bin lengths shown in Fig. 2. The SM-NL and ML-NS events produced small enhancements (79 kJ m^{-2} and 71.6 kJ m^{-2}, respectively) compared to the ML-S events (561 kJ m^{-2}) since the SM-NL and ML-NS events were associated with much shorter timescales compared to the ML-S events. For all three types of convective organization, the majority of the sensible heat transfer occurred during the recovery, attributed primarily to significant air–sea temperature differences (term ii) over an extended period of time. The large sensible heat fluxes during the convectively active phase accounted for between 31.1% and 39.9% of the total sensible heat transfer enhancement.

c. Latent heat flux enhancements

Table 6 shows the total latent heat flux enhancements along with its decomposition into the seven terms on the right-hand side of (3b). The largest enhancements are confined to the convectively active periods for all three types of convective organization since the greatest wind speeds were observed during those periods. For the SM-NL events, the enhanced latent heat flux was due almost entirely to increased wind speed (term i). Both the air–sea humidity difference (term ii) and the transfer coefficient for moisture (term iii) decrease slightly in response to the convective activity, thereby acting to limit the latent heat flux enhancement. The ML-NS events did produce a weak increase in the air–sea humidity difference near the end of the convectively active phase and early in the recovery phase. Therefore, weak contributions from terms ii and iv were present during those periods.

For the ML-S events, the primary contributor to the enhanced latent heat fluxes during the convectively active periods was increased wind speed (term i), accounting for over half of the total enhancement. However, increased air–sea humidity difference (term ii) and

TABLE 5. The enhancements of sensible heat transferred from the ocean to the atmosphere during the convectively active (CA) and recovery (REC) periods, decomposed into the individual terms on the right-hand side of Eq. 3a. The breakdown of enhancements for (a) SM-NL, (b) ML-NS, and (c) ML-S composites, along with their total enhancements (TE), are shown. Values are in kJ m^{-2}. Values in parentheses indicate the percentage of the total enhancement.

Period	Term i	Term ii	Term iii	Term iv	Term v	Term vi	Term vii	TE_{SH}
				(a) SM-NL				
CA	13.9 (17.7%)	9.7 (12.2%)	−1.3 (−1.7%)	11.2 (14.1%)	−1.1 (−1.4%)	−1.5 (−1.9%)	−1.3 (−1.7%)	29.5 (37.4%)
REC	18.6 (23.6%)	27.7 (35.1%)	−3.7 (−4.7%)	11.7 (14.8%)	−2.2 (−2.7%)	−1.5 (−2.1%)	−1.1 (−1.5%)	49.5 (62.6%)
				(b) ML-NS				
CA	9.4 (13.2%)	11.1 (15.5%)	0.2 (0.3%)	7.2 (10.1%)	0.3 (0.4%)	0.2 (0.2%)	0.2 (0.2%)	28.6 (39.9%)
REC	8.9 (12.4%)	26.9 (37.5%)	0.9 (1.2%)	5.5 (7.7%)	0.6 (0.9%)	0.2 (0.2%)	0.2 (0.2%)	43.0 (60.1%)
				(c) ML-S				
CA	15.7 (2.8%)	94.7 (16.9%)	3.0 (0.5%)	47.0 (8.4%)	8.6 (1.5%)	1.4 (0.2%)	4.4 (0.8%)	174.5 (31.1%)
REC	−16.4 (−2.9%)	373.6 (66.6%)	11.5 (2.0%)	−4.4 (−0.8%)	22.3 (4.0%)	−0.5 (−0.1%)	0.4 (0.1%)	386.5 (68.9%)

the simultaneous increase in wind speed and air–sea humidity difference (term iv) also contributed significantly, accounting for about 20% and 10% of the enhancement, respectively. Increases in the transfer coefficient for moisture (term iii) also accounted for about 10% of the latent heat flux enhancement. During the recovery periods for the ML-S events, increased air–sea humidity difference was the primary contributor, with an enhanced transfer coefficient for moisture also weakly contributing to the total latent heat flux enhancement. During the last four recovery bins, the wind speed was less than the preconvective wind speed, thereby greatly limiting the latent heat flux enhancements.

The partitioned enhancement in heat transfer from the ocean to the atmosphere via latent heat fluxes during the convectively active and recovery phases is summarized in Table 7. As with the sensible heat flux, the SM-NL and ML-NS events produced small latent heat transfer enhancements (284.2 kJ m^{-2} and 335.6 kJ m^{-2}, respectively) compared to the ML-S events (1091.5 kJ m^{-2}). For the SM-NL events, nearly 60% of the heat transfer associated with enhanced latent heat fluxes occurred during the convectively active phase and only about 40% occurred during the recovery phase, due almost entirely to increased wind speeds. For the MCS-scale linear events, the enhanced heat transfer was split nearly evenly between the convectively active and recovery phases. During the convectively active phases of these events, an increase in wind speed was the primary contributor, with the increased air–sea humidity difference contributing weakly for the ML-S events. During the recovery phase, the effect of increased air–sea humidity difference accounted for approximately 55% of the total enhanced latent heat transfer for the ML-S, whereas enhancements in the transfer coefficient for moisture accounted for about 20%. For the ML-NS events, weak wind speed enhancements during the recovery phase accounted for about 40% of the total latent heat transfer enhancement.

5. Conclusions

The goal of this study was to provide a detailed description of how the three types of convective organization most frequently observed during TOGA COARE modulate the surface fluxes of heat, moisture, and momentum. Previous studies have explored the effects of convective systems on the boundary layer, however, these earlier studies did not systematically quantify the boundary layer's response to different modes of convective organization. Our study has shown that the response of the boundary layer in the TOGA COARE region is highly sensitive to the mode of convective organization.

The average length of the convectively active phase ranged from about 45 min for the ML-NS events to over 90 min for the ML-S events. The average duration of the recovery phase varied even more with convective

TABLE 6. Same as Table 4 except the decomposition of the latent heat flux enhancements into the individual terms on the right-hand side of Eq. (3b).

Period	Term i	Term ii	Term iii	Term iv	Term v	Term vi	Term vii	TE_{LH}
				(a) SM-NL				
CA1	44.83	−0.80	−3.93	−0.54	0.05	−2.62	0.03	37.02
CA2	89.23	−0.83	−7.66	−1.11	0.10	−10.18	0.13	69.68
CA3	74.86	0.82	−9.09	0.92	−0.11	−10.14	−0.12	57.12
REC1	43.26	−2.29	−7.81	−1.48	0.27	−5.03	0.17	27.09
REC2	27.03	−3.23	−6.59	−1.30	0.32	−2.65	0.13	13.70
REC3	9.77	−4.63	0.22	−0.67	−0.02	0.03	0.00	4.69
REC4	8.25	−7.42	−1.82	−0.91	0.20	−0.22	0.02	−1.90
REC5	19.73	−9.25	−5.94	−2.72	0.82	−1.75	0.24	1.14
				(b) ML-NS				
CA1	52.80	0.27	−0.47	0.18	0.00	−0.30	0.00	52.48
CA2	65.61	2.70	1.67	2.17	0.06	1.33	0.04	73.58
CA3	45.75	7.66	2.05	4.28	0.19	1.14	0.11	61.17
REC1	19.61	7.54	2.67	1.80	0.25	0.64	0.06	32.56
REC2	15.78	3.11	1.69	0.60	0.06	0.33	0.01	21.59
REC3	15.63	1.99	0.66	0.38	0.02	0.13	0.00	18.81
REC4	12.36	−0.43	1.47	−0.07	−0.01	0.22	0.00	13.54
REC5	10.98	−4.60	0.66	−0.62	−0.04	0.09	0.00	6.47
				(c) ML-S				
CA1	30.09	10.37	7.03	2.49	0.58	1.69	0.14	52.40
CA2	61.64	21.23	12.81	10.44	2.17	6.30	1.07	115.65
CA3	73.18	30.45	12.31	17.78	2.99	7.19	1.75	145.63
REC1	15.55	22.84	10.26	2.83	1.87	1.27	0.23	54.86
REC2	−5.89	24.78	8.92	−1.16	1.76	−0.42	−0.08	27.90
REC3	−7.39	23.27	4.46	−1.37	0.83	−0.26	−0.05	19.48
REC4	−23.13	12.45	3.10	−2.30	0.31	−0.57	−0.06	−10.20
REC5	−25.90	5.58	7.84	−1.15	0.35	−1.62	−0.07	−14.98

organization. For the SM-NL and ML-NS events, the recovery phase was relatively short, approximately 3.5 and 2.5 h, respectively, whereas for the ML-S events, the recovery phase was much longer, approximately 9 h. This was due in large part to the ML-S events producing greater air temperature depressions (Fig. 5c) than the other types of events, which can be related to the overall intensity of the convective elements. The ML-S events were also associated with a significant stratiform component that likely limited the rate at which the boundary layer air temperature recovered to its undisturbed environmental value due to evaporational cooling below cloud base and a reduction in solar insolation. The average length of the convective wakes presented by Young et al. (1995) was 12.7 h only slightly longer than our finding for the ML-S events. It should be noted that Young et al. limited their study to convective wakes lasting 6 h or longer.

The SM-NL events developed in environmental conditions that limited their vertical development and upscale growth (Rickenbach and Rutledge 1998). These events typically had short lifetimes (typically 1 h or less), limiting their impact on the surface fluxes. These events produced relatively weak increases in wind speed and air–sea temperature difference (i.e., decreased air temperature), but did not produce any significant changes in specific humidity. Addis et al. (1984) observed many convectively induced gust fronts during GATE that did not have any significant decreases in specific humidity associated with them, in fact a good number of their cases showed increases in the specific humidity, but in general all of the cases had air temperature depressions and wind speed enhancements associated with them. This behavior is also similar to the light rain cases described by Barnes and Garstang (1982), who hypothesized that the lighter rain cases in their study lacked strong, penetrative convective-scale downdrafts. It should be noted that Addis et al. and Barnes and Garstang did not consider different types of convective organization in their studies. The ML-NS events, which were indicative of developing squall lines or MCS-scale lines that were not highly organized, produced responses very similar to the SM-NL events. The more highly organized and mature ML-S events produced very large responses at the surface, including large enhancements in the wind speeds, air–sea temperature differences, along with air–sea humidity differences.

The peak wind stress value in the ML-S composite (0.2 N m^{-2}) was a factor of two and four greater than those in the ML-NS and SM-NL composites, respectively, while the peak sensible heat flux value in the ML-S composite (60 W m^{-2}) was about a factor of three greater than in the composites for the other two classifications. In the ML-S latent heat flux composite, the peak value was 250 W m^{-2}, whereas for the SM-NL and ML-NS events, the peak values were only about 135 W m^{-2} and 150 W m^{-2}, respectively. The ML-S

TABLE 7. Same as Table 5 except the enhancements of latent heat transferred from the ocean to the atmosphere, decomposed into the individual terms on the right-hand side of Eq. (3b).

Period	Term i	Term ii	Term iii	Term iv	Term v	Term vi	Term vii	TE_{LH}
				(a) SM-NL				
CA	212.4 (74.7%)	−0.8 (−0.3%)	−21.0 (−7.4%)	−0.7 (−0.3%)	0.0 (0.0%)	−23.3 (−8.2%)	0.0 (0.0%)	166.6 (58.6%)
REC	284.1 (100.0%)	−70.5 (−24.8%)	−57.7 (−20.3%)	−18.6 (−6.6%)	4.2 (1.5%)	−25.3 (−8.9%)	1.5 (0.5%)	117.6 (41.4%)
				(b) ML-NS				
CA	145.0 (43.2%)	9.4 (2.8%)	2.9 (0.9%)	5.8 (1.7%)	0.2 (0.1%)	1.9 (0.6%)	0.1 (0.0%)	165.4 (49.3%)
REC	136.1 (40.6%)	13.9 (4.2%)	13.1 (3.9%)	3.8 (1.1%)	0.5 (0.2%)	2.6 (0.8%)	0.1 (0.0%)	170.2 (50.7%)
				(c) ML-S				
CA	301.3 (27.6%)	113.4 (10.4%)	58.7 (5.4%)	56.1 (5.1%)	10.5 (1.0%)	27.7 (2.5%)	5.4 (0.5%)	573.2 (52.5%)
REC	−314.5 (−28.8%)	598.0 (54.8%)	232.5 (21.3%)	−21.2 (−1.9%)	34.4 (3.2%)	−10.8 (−1.0%)	−0.2 (0.0%)	518.3 (47.5%)

events also produced greater rain rates than the other two convective classifications, which, combined with the greater air–sea temperature differences, lead to the ML-S events producing peak rainfall heat flux values (75 W m^{-2}) over twice as large as the other classifications.

Despite the fact that the ML-S events produced the greatest enhancements in the surface fluxes, the largest SST changes were induced by the relatively weak forcing associated with the SM-NL systems. The SST is controlled to a large extent by the state of the upper ocean, so therefore the larger SST changes may not be associated with the largest surface forcing. ML-S events tended to develop during periods of strong winds, when the oceanic mixed layer was relatively deep and the enhanced forcing associated with convective systems apparently was not strong enough or of sufficient duration to significantly modify this relatively deep layer of water. Hence, the SST did not change significantly. The SM-NL systems, on the other hand, tended to develop during periods of limited cloud cover and weak winds. Such a combination is conducive to the formation of a shallow, near-surface warm layer (Lukas 1991). This warm layer is typically on the order of meters deep and therefore is very sensitive to any enhanced forcing (Price et al. 1986). Since the SM-NL events tended for development during these periods, the weak surface flux enhancements associated with them, in turn, led to significant changes in the SST.

For all three types of convective organization, the enhanced sensible heat fluxes during the convectively active phase was due to the combined effects of increased wind speeds and increased air–sea temperature differences. The increased wind speed during this phase was also the primary contributor to the enhanced latent heat fluxes. However, for the ML-S events, increases in the air–sea humidity difference, and the transfer coefficient for moisture also made significant contributions. During the recovery phase, the sensible heat flux enhancements were due almost entirely to increased air–sea temperature differences. The latent heat flux enhancements during this phase were attributable to weak increases in wind speed for the SM-NL and ML-NS events. However, for the ML-S events, increases in the air–sea humidity difference, and to a lesser extent the transfer coefficient for moisture were the primary contributors. During the last half of the recovery phase, the wind speed subsided to less than the preconvective value in the ML-S composites, thereby limiting the surface flux enhancements during this period. This same wind speed behavior can be seen in the analysis of a GATE squall line by Gamache and Houze (1982) and Johnson and Nicholls (1983).

For all three types of convective organization, the majority of the enhanced sensible heat transfer occurred during the recovery phase (Table 5) since all classifications produced significant increases in air–sea temperature difference, which acted to enhance the sensible

heat fluxes over an extended period of time during the recovery phase. The large sensible heat flux enhancements during the convectively active phase occurred for only a short period of time relative to the recovery phase, thereby limiting their effect. It is interesting to note, especially for the ML-S events, that the enhanced sensible heat transfer (561 kJ m^{-2}) is not negligible compared to the enhanced latent heat transfer (1091.5 kJ m^{-2}). Therefore, especially for these larger systems, enhancements in the sensible heat flux should not be neglected.

The majority of the enhanced latent heat transfer (about 60%) occurred during the convectively active phase for the SM-NL events, whereas for the MCS-scale events, the enhanced latent heat transfer was evenly divided between the convectively active and recovery phases. Enhanced air–sea humidity differences were only observed in the ML-S events, resulting in weak latent heat flux enhancements during the majority of the recovery phase. The presence of mesoscale downdrafts below the stratiform precipitation would allow drier air to be entrained into the boundary layer early in the recovery phase (Zipser 1977). Since the SM-NL and ML-NS events did not have significant stratiform precipitation associated with them, this effect would not be expected for those events and indeed it was not observed.

Many of the conclusions outlined above are consistent with previous studies; namely, that convective activity leads to greatly enhanced surface fluxes (e.g., Johnson and Nicholls 1983; Addis et al. 1984; Young et al. 1995; Jabouille et al. 1996), that wind speed enhancements are mostly confined to the convectively active regions (Jabouille et al. 1996), and that the sensible heat flux enhancements are due to the combined effects of increased wind speed and air–sea temperature difference (e.g., Johnson and Nicholls 1983; Young et al. 1995; Jabouille et al. 1996). However, many previous studies reported that the effects of increased air–sea humidity difference are negligible (Addis et al. 1984; Young et al. 1995; Jabouille et al. 1996). The results reported in this study show that while the effects of increased wind speed are the most significant contributor to the enhanced latent heat flux during the convectively active phase, the effects of enhanced air–sea humidity difference do make significant contributions to the latent heat flux enhancements for the ML-S convective events, especially early in the recovery phase. The results also suggest that since the air–sea temperature difference remains enhanced for such an extended period of time (especially in the ML-S events), the net result of this enhancement is not negligible when compared to the increase in the heat transfer associated with the latent heat flux.

Acknowledgments. Drs. Robert Weller and Steven Anderson are acknowledged for providing the IMET buoy data collected during COARE. We would also like to thank Dr. Walt Petersen and three anonymous reviewers for their comments and suggestions on an earlier version of this manuscript. We also acknowledge all personnel who so skillfully operated the MIT radar during COARE. This research was supported by TOGA COARE Grants NA90RAH00077 and NA37RJ0202 from the National Oceanic and Atmospheric Administration Office of Global Programs.

REFERENCES

Addis, R. P., M. Garstang, and G. D. Emmitt, 1984: Downdrafts from tropical oceanic cumuli. *Bound.-Layer Meteor.,* **28,** 23–49.

Barnes, G. M., and M. Garstang, 1982: Subcloud layer energies of precipitating convection. *Mon. Wea. Rev.,* **110,** 102–117.

——, and K. Sieckman, 1984: The environment of fast- and slow-moving tropical mesoscale convective cloud lines. *Mon. Wea. Rev.,* **112,** 1782–1794.

Betts, A. K., R. W. Grover, and M. W. Moncrieff, 1976: Structure and motion of tropical squall-lines over Venezuela. *Quart. J. Roy. Meteor. Soc.,* **102,** 395–404.

Bruce, J. G., and E. Firing, 1974: Temperature measurements in the upper 10 m with modified expendable bathythermograph probes. *J. Geophys. Res.,* **79,** 4110–4111.

Fairall, C. W., E. F. Bradley, J. S. Godfrey, G. A. Wick, J. B. Edson, and G. S. Young, 1996a. Cool-skin and warm-layer effects on sea surface temperature. *J. Geophys. Res.,* **101,** 1295–1308.

——, ——, D. P. Rogers, J. B. Edson, and G. S. Young, 1996b: Bulk parameterization of air–sea fluxes for Tropical Ocean Global Atmosphere Coupled Ocean–Atmosphere Response Experiment. *J. Geophys. Res.,* **101,** 3747–3764.

Flament, P., and M. Sawyer, 1995: Observations of the effect of rain temperature on the surface heat flux in the intertropical convergence zone. *J. Phys. Oceanogr.,* **25,** 413–419.

Gamache, J. F., and R. A. Houze Jr., 1982: Mesoscale air motions associated with a tropical squall line. *Mon. Wea. Rev.,* **110,** 118–135.

Gaynor, J. E., and C. F. Ropelewski, 1979: Analysis of the convectively modified GATE boundary layer using in situ and acoustic sounder data. *Mon. Wea. Rev.,* **107,** 985–993.

Gosnell, R., C. W. Fairall, and P. J. Webster, 1995: The sensible heat of rainfall in the tropical ocean. *J. Geophys. Res.,* **100,** 18 437–18 442.

Houze, R. A., 1993: *Cloud Dynamics.* Academic Press, 573 pp.

Jabouille, P., J. L. Redelsperger, and J. P. Lafore, 1996: Modification of surface fluxes by atmospheric convection in the TOGA COARE region. *Mon. Wea. Rev.,* **124,** 816–837.

Johnson, R. H., and M. E. Nicholls, 1983: A composite analysis of the boundary layer accompanying a tropical squall line. *Mon. Wea. Rev.,* **111,** 308–319.

Kinzer, G. D., and R. Gunn, 1951: The evaporation, temperature, and thermal relaxation-time of freely falling water drops. *J. Meteor.,* **8,** 71–83.

Ledvina, D. V., G. S. Young, R. A. Miller, and C. W. Fairall, 1993: The effect of averaging on bulk estimates of heat and momentum fluxes for the tropical western Pacific Ocean. *J. Geophys. Res.,* **98,** 20 211–20 217.

Liu, W. T., K. B. Katsaros, and J. A. Businger, 1979: Bulk parameterization of air–sea exchanges of heat and water vapor including the molecular constraints at the interface. *J. Atmos. Sci.,* **36,** 1722–1735.

Lukas, R., 1991: The diurnal cycle of sea surface temperature in the western equatorial Pacific. *TOGA Notes,* **2,** 1–5.

Patterson, V. L., M. D. Hudlow, P. J. Pytlowany, F. P. Richards, and J. D. Hoff, 1979: GATE radar rainfall processing system. NOAA Tech. Memo. EDIS 26, NOAA, Washington, DC, 34 pp. [Available from National Technical Information Service, Sills Building, 5285 Port Royal Road, Springfield, VA 22161.]

Pickard, G. L., and W. J. Emery, 1990: *Descriptive Physical Oceanography.* Pergamon Press, 320 pp.

Price, J. F., 1979: Observations of a rain-formed mixed layer. *J. Phys. Oceanogr.,* **9,** 643–649.

——, R. A. Weller, and R. Pinkel, 1986: Diurnal cycling: Observations and models of the upper ocean response to diurnal heating, cooling, and wind mixing. *J. Geophys. Res.,* **91,** 8411–8427.

Rickenbach, T. M., and S. A. Rutledge, 1998: Convection in TOGA COARE: Horizontal scale, morphology, and rainfall production. *J. Atmos. Sci.,* **55,** 2715–2729.

Rotunno, R., J. B. Klemp, and M. L. Weismann, 1988: A theory for strong, long-lived squall lines. *J. Atmos. Sci.,* **45,** 463–484.

Rutledge, S. A., R. Cifelli, C. DeMott, W. Peterson, T. Rickenbach, J. Lutz, R. Bowie, M. Strong, and E. Williams, 1993: The shipboard deployment of the MIT C-band radar during TOGA COARE. Preprints, *26th Int. Conf. on Radar Meteorology*, Norman, OK, Amer. Meteor. Soc., 371–373.

Short, D. A., P. A. Kucera, B. S. Ferrier, J. C. Gerlach, S. A. Rutledge, and O. W. Thiele, 1997: Shipboard radar rainfall patterns within the TOGA COARE IFA. *Bull. Amer. Meteor. Soc.,* **78,** 2817–2836.

Steiner, M., and R. A. Houze Jr., 1993: Three-dimensional validation at TRMM ground truth sites: Some early results from Darwin, Australia. Preprints, *26th Int. Conf. on Radar Meteorology*, Norman, OK, Amer. Meteor. Soc., 417–420.

——, ——, and S. E. Yuter, 1995: Climatological characteristics of three-dimensional storm structure from operational radar and raingauge data. *J. Appl. Meteor.,* **34,** 1978–2007.

Taylor, R., 1973: *An Atlas of Pacific Rainfall.* Hawaii Institute of Geophysics Rep. HIG-73-9, 7 pp. [Available from Hawaii Institute of Geophysics, 2525 Correa Road, Honolulu, HI 96822.]

Tokay, A., and D. A. Short, 1996: Evidence from tropical raindrop spectra of the origin of rain from stratiform versus convective clouds. *J. Appl. Meteor.,* **35,** 355–371.

Tomczak, M., 1995: Salinity variability in the surface layer of the tropical western Pacific Ocean. *J. Geophys. Res.,* **100,** 20 499–20 515.

Trier, S. B., W. C. Skamarock, M. A. LeMone, D. B. Parsons, and D. P. Jorgensen, 1996: Structure and evolution of the 22 February 1993 TOGA COARE squall line: Numerical simulations. *J. Atmos. Sci.,* **53,** 2861–2886.

Webster, P. J., and R. Lukas, 1992: TOGA COARE: The Coupled Ocean–Atmosphere Response Experiment. *Bull. Amer. Meteor. Soc.,* **73,** 1377–1416.

Weller, R. A., and S. P. Anderson, 1996: Surface meteorology and air–sea fluxes in the western equatorial Pacific warm pool during the TOGA Coupled Ocean–Atmosphere Response Experiment. *J. Climate,* **9,** 1959–1990.

Young, G. S., S. M. Perugini, and C. W. Fairall, 1995: Convective wakes in the equatorial western Pacific during TOGA. *Mon. Wea. Rev.,* **123,** 110–123.

Zipser, E. J., 1969: The role of organized unsaturated convective downdrafts in the structure and rapid decay of an equatorial disturbance. *J. Appl. Meteor.,* **8,** 799–814.

——, 1977: Mesoscale and convective-scale downdrafts as distinct components of squall line structure. *Mon. Wea. Rev.,* **105,** 1568–1589.